

Detection and analysis of cloud boundary in Xi'an, China employing 35GHz cloud radar aided by 1064nm lidar

Yun Yuan , Huige Di *, Yuanyuan Liu , Tao Yang , Qimeng Li, Qing Yan, Wenhui Xin, Shichun Li, Dengxin Hua*

School of Mechanical and Precision Instrument Engineering, Xi'an University of Technology, Xi'an 710048, China

* Corresponding author: dihuige@xaut.edu.cn, dengxinhua@xaut.edu.cn

Lidar @1064 nm and Ka-band millimeter-wave cloud radar (MMCR) are powerful tools for detecting the height distribution of cloud boundaries, and can monitor the entire life cycle of cloud layers. In this study, lidar and MMCR are employed to jointly detect cloud boundaries under different conditions. By enhancing the echo signal of lidar @1064 nm and combining its Signal-to-noise ratio (SNR), the cloud signal can be accurately extracted from the aerosol signals and background noise. The interference signal is eliminated from Doppler spectra of the MMCR by using the noise ratio of the smallest measurable cloud signal (SNR_{min}) and the spectral point continuous threshold (N_{ts}). Moreover, the quality control of the reflectivity factor of MMCR obtained by the inversion is conducted, which improves the detection accuracy of the cloud signal. We analyzed three typical cases studies; case one presents two interesting phenomena: a) at 19:00–20:00 CST (China standard time), the ice crystal particles at the cloud top boundary are too small to be detected by MMCR, but they are well detected by lidar. b) at 19:00–00:00 CST, the cirrus cloud tranists to altostratus where the cloud particles eventually grow into large sizes, producing precipitation. Further, MMCR has more advantages than lidar in detection the cloud top boundary within this period. Considering the advantages of the two devices, the change characteristics of the cloud boundary in Xi'an from December 2020 to November 2021 were analysed, with MMCR detection data as the main data and lidar data as the assistant data. The seasonal variation characteristics of clouds show that, in most cases, high clouds often occur in summer and autumn, and the low clouds are usually in winter. The normalised cloud cover shows that the maximum and minimum cloud cover occur in summer and winter, respectively. Furthermore, the cloud boundary frequency distribution results for the whole of observation period show that the cloud bottom boundary below 1.5 km is more than 1%, the frequency within the height range of 3.06–3.6 km is approximately 0.38%, and the frequency above 8 km is less than 0.2%. The cloud top boundary frequency distribution exhibits the characteristics of a bimodal distribution. The first narrow peak lies at approximately 1.0–3.1 km, and the second peak appears at 6.4–9.8 km.

Keywords: Cloud detection; cloud boundary; Lidar; Ka-band millimeter-wave cloud radar (MMCR); Frequency distribution; Remote sensing and sensors

1 Introduction

A cloud is a mixture of water droplets or ice crystals suspended in the air at a certain height through condensation or condensing after the water vapour in the atmosphere reaches saturation (Wang et al., 1998; Zhou et al., 2016; Wild et al., 2012; Stephens et al., 2012). Cloud vertical structure information (Thorsen et al., 2013; Lohmann et al., 2017; Stephens et al., 2005; Wang et al., 1995; Nakajima et al., 1991) reflects the thermodynamic and dynamic processes of the atmosphere and participates in the global water cycle through formation, development, movement,

37 and dissipation (Wild et al., 2012; Zhang et al., 2012; Zhang et al., 2017; Sherwood et al., 2014; Dong et al., 2010).
38 However, the vertical structure distribution of clouds has great temporal and spatial heterogeneity and a high rate of
39 change, which leads to great challenges in accurately evaluating the radiation effects of clouds at different cloud
40 types and heights. Research on the characteristics of vertical cloud structures has always been an important
41 direction in cloud physics research (Zcab et al., 2019). Cloud boundaries are the main information in the study of
42 vertical cloud structure, mainly referring to the cloud bottom and top boundaries, including the side boundary. The
43 cloud boundary in this study mainly refers to the cloud bottom and top boundaries. Multilayer clouds also include
44 boundary information of intermediate discontinuous clouds (Zhou et al., 2019; Varikoden et al., 2011; Li et al.,
45 2013; Ward et al., 2004; Zhang et al., 2018; Kuji et al., 013; Kitova et al., 003; Cao et al., 021). With the
46 development of remote sensing detection technology, Ka-band millimeter-wave cloud radar (MMCR) (Görsdorf et
47 al., 2015; Kollias et al., 2017; Kollias et al., 2007) and lidar (Apituley et al., 2000; Protat et al., 2011; Motty et al.,
48 2018; Cordoba et al., 2017) have become effective instruments for cloud boundary detection.

49 Common methods for detecting cloud boundaries using lidar include the threshold method and differential
50 zero-crossing method. The threshold method (Kovalev et al., 2005) uses a background signal to measure the echo
51 signal amplitude. The first point where the echo signal is higher than the background signal and exceeds the set
52 threshold is the cloud bottom boundary. However, because of the existence of noise, a point with a marked increase
53 in amplitude may not be found under the condition of a low signal-to-noise ratio (SNR); therefore, the cloud bottom
54 boundary cannot be judged. Pal et al. (1992) proposed the differential zero-crossing method through Calculation of
55 dP/dr using lidar backscattering intensity P and range r , and the first derivative of backscatter intensity dP/dr
56 changes sign from negative to positive and this zero crossing is cloud bottom. The threshold, differential
57 zero-crossing, and variant detection methods are all based on the feature points of cloud boundaries (Streicher et al.,
58 1995). They are easily affected by noise, and some indicators must be introduced in the specific implementation
59 process to determine the cloud boundary by changing the experience threshold frequently during calculation, which
60 causes difficulties in accurate cloud boundary detection. Young et al. (1995) designed an independent
61 double-window algorithm to detect cloud bottom and top boundaries by combining the lidar signal and a known
62 atmospheric backscatter signal. However, the algorithm needs to manually adjust the window size or the selection
63 of the threshold. Based on the wavelet covariance transform method, Morille et al. (2007) determined the local
64 maxima on both sides of the cloud peak as cloud bottom and cloud top, but this method takes some real signals at
65 the cloud bottom as noise and miss information at the cloud top, and resulting in overestimation and underestimated
66 of cloud base and cloud top height respectively. Mao (2011) adopted a multiscale hierarchical detection algorithm,
67 selected the starting and ending points of the feature area as the cloud bottom and cloud peak, and detected the
68 cloud top and bottom through multiple iterative updates.

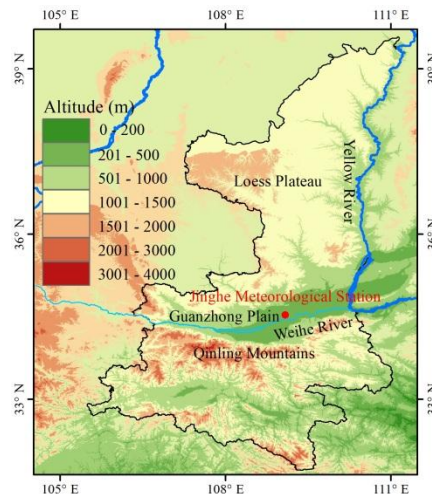
69 The determination of the cloud boundary by MMCR is mainly based on the threshold of the echo reflectivity factor
70 used to detect the cloud boundary (Hobbs et al., 1985; Platt et al., 1994). Kollias et al. (2007) judge step by step
71 from the bottom to the top of the reflectivity. If the SNR of more than nine consecutive distance gates reaches the
72 set threshold, these gates represented as cloud signals; otherwise, it is deemed a noncloud signal. Clothiaux et al.
73 (1999) used 35 GHz millimeter wave cloud measuring radar to analyse different types of clouds and considered that
74 the dynamic range of the cloud reflectivity factor is from -50 to 20 dBZ. The existence of certain ground object

75 echoes and biological groups (including insects and other biological particles) in the lower atmosphere interferes
76 with real cloud echo signals (Luke et al., 2008; G6rsdorf et al., 2015; Oh et al., 2016; Melnikov et al., 2013;
77 Melnikov et al., 2015). If the subjective reflectivity factor threshold is directly used to determine the cloud signal, it
78 is not suitable for all cloud types. Therefore, when a cloud signal cannot be accurately identified, large errors in the
79 detection of cloud boundaries result.

80 Research on the macro- and microscopic structures of clouds in a specific area mainly relies on ground-based
81 observations. Currently, for better cloud detection, it is necessary to combine lidar and MMCR to observe and study
82 local clouds (Sauvageot et al., 1996; Intrieri et al., 1993; Wang et al., 2000; Sasse et al., 2001; Borg et al., 2011;
83 Delano6 and Hogan, 2008). This study combined the advantages of lidar and MMCR in detecting clouds to achieve
84 high-precision cloud boundary detection and inversion. We effectively identify cloud signals from Doppler spectra
85 data of MMCR, and through data quality control, the interference signal caused by floating debris is eliminated to
86 improve the detection accuracy of the cloud boundary. Based on the idea that the MMCR only presents the cloud
87 signal to make cloud boundary detection simple and easy to operate, in this study, we effectively separate the cloud
88 signal from aerosol and background noise by enhancing and transforming the lidar signal and combining the SNR
89 (Xie et al., 2017) to realise the accurate detection of cloud boundaries. By analysing the results of cloud boundary
90 detection by the two instruments under special weather conditions in Xi'an, the cloud boundary evaluation criteria
91 for the joint observation of the two instruments are established, and the variation characteristics of cloud boundary
92 height over Xi'an in 2021 are statistically analysed in detail.

93 2 Observation and Instrument

94 Xi'an City (107°40'-109°49'E, 33°42'-34°45'N), Shaanxi Province (105°29'-111°15'E, 31°42'-39°35'N) is
95 located in the Guanzhong Basin in the middle of the Weihe River Basin, bordering the Weihe River and Loess
96 Plateau to the north and the Qinling Mountains to the south. Xi'an has a semi-humid climate. Owing to its special
97 geographical location, it is particularly urgent to analyse cloud observations and analyses in Xi'an. The lidar and
98 MMCR are installed at the Jinghe National Meteorological Station in China, placed side-by-side at a distance of 50
99 m, and both adopt the vertical observation mode to obtain the vertical structure information of clouds. Black line
100 represents Shaanxi Province, dark blue represents the Yellow River, wathet blue represents the Weihe River, and
101 red dot indicates the location of the Jinghe National Meteorological Station in Fig. 1.



102
103 Fig. 1. Geographical coverage of Shaanxi Province (105°29'-111°15'E, 31°42'-39°35'N). The red dot indicates the location of the
104 Jinghe National Meteorological Station in Xi'an (107°40'-109°49'E, 33°42'-34°45'N).

105 The lidar used in this study was developed by Xi'an University of Technology. The MMCR is the HT101
 106 all-solid-state cloud radar researched by Xi'an Huateng Microwave Co., Ltd. The main parameters are listed in
 107 Tables 1 and 2, respectively.

108 Table 1 Main parameters of the lidar

Indicators	Devices	Main parameter
Launch system	Laser	Nd:YAG; 0.75J@1064nm
Receiving system	Cassegrain telescope	Φ400 mm
	Filter	0.5 nm
Detection system	Detector	APD
	Sampling mode	Analog detection
Spatiotemporal resolution	Time resolution	2 min
	Range resolution	3.75 m
	Pulse accumulation	2000

109
 110 Table 2 Main parameters of MMCR

Indicators	Detailed description	
Radar system	All solid-state; All coherent Doppler; Pulse compression	
Working frequency	35 GHz, and wavelength is 8.6 mm	
Detection altitude range	15 km	
Detection blind area	150 m	
Spatiotemporal resolution	Time resolution	5 s
	Range resolution	30 m
Scanning mode	Vertical headspace fixed pointing	
Pulse width	1 μs、5 μs、20 μs	
Detection accuracy	$Z \leq 0.5 \text{ dB}$ 、 $V \leq 0.5 \text{ m/s}$ 、 $W \leq 0.5 \text{ m/s}$	

111 3 Method

112 Using active instruments to determine cloud boundaries through remote sensing measurements, echo signals in
 113 clear-sky areas decay rapidly with increasing detection distance. When a cloud signal is detected, the amplitude of
 114 the echo signal begins to increase sharply. Usually, [during the actual observation](#), the background noise or aerosol
 115 layer also increases the amplitude of the echo signal, but the backscattering intensity of the cloud layer is more
 116 continuous and stronger than the aerosol layer and background noise. Therefore, cloud layer and cloud boundary
 117 detection can be realised according to the characteristic changes [in](#) the echo signals.

118 3.1 Lidar cloud boundary detection

119 The lidar equation owing to elastic backscattering (Wandinger, 2005; Motty et al., 2018) can be written as,
 120

$$P(\lambda, r) = P_0 \frac{c\tau}{2} A\eta \frac{O(r)}{r^2} \beta(\lambda, r) \cdot \exp\left[-2\int_0^r \sigma(\lambda, r) dr\right], \quad (1)$$

121 where λ is the wavelength of the emitted light, r represents the detection distance, and $\beta(\lambda, r)$ and $\sigma(\lambda, r)$ are the
 122 atmospheric backscattering and extinction coefficients, respectively. $O(r)$ is the laser-beam receiver field-of-view

123 overlap function, c is the speed of light, P_0 is the average power of a single laser pulse, τ is the temporal pulse
 124 length, η is the overall system efficiency, and A is the area of the primary receiver optics responsible for the
 125 collection of backscattered light.

126 Considering the influence of the background noise and response noise of the photomultiplier detector, Eq. (1) can
 127 be further expressed as

$$128 \quad P(\lambda, r) = C \cdot \frac{\Delta r}{r^2} \cdot \beta(\lambda, r) \cdot \exp\left[-2 \int_0^r \sigma(\lambda, r) dr\right] + E(\lambda, r) + N_{back}(\lambda, r'), \quad (2)$$

129 where C is the system constant, which is determined by the laser energy, receiving area of the telescope, and
 130 quantum efficiency of the detector. Δr is the detection range resolution of the system. $N_{back}(\lambda, r')$ is the background
 131 noise received by the system. $E(\lambda, r)$ represents the noise introduced to the detection system by calibration.

132 To avoid amplifying the high-level noise signals, we do not perform distance square correction in Eq. (2) but
 133 directly process it as follows:

$$134 \quad P_{new}(\lambda, r) = \frac{P(\lambda, r) - E(\lambda, r) - N_{back}(\lambda, r')}{C \cdot \Delta r}. \quad (3)$$

135 For ground-based lidar, the echo signal at a certain height range (>15 km in this study applied to the Xi'an region)
 136 can be considered as molecular scattering, $N_{back}(\lambda, r')$ can be estimated with the signal within this range, and the
 137 standard deviation of the noise within the distance range is calculated as follows:

$$138 \quad Sd = \left[\frac{1}{n-1} \sum_{i=1}^n \left(x_i - \frac{1}{n} \sum_{i=1}^n x_i \right) \right]^2, \quad (4)$$

139 where x denotes the background noise signal. The noise of the lidar signal can be expressed as

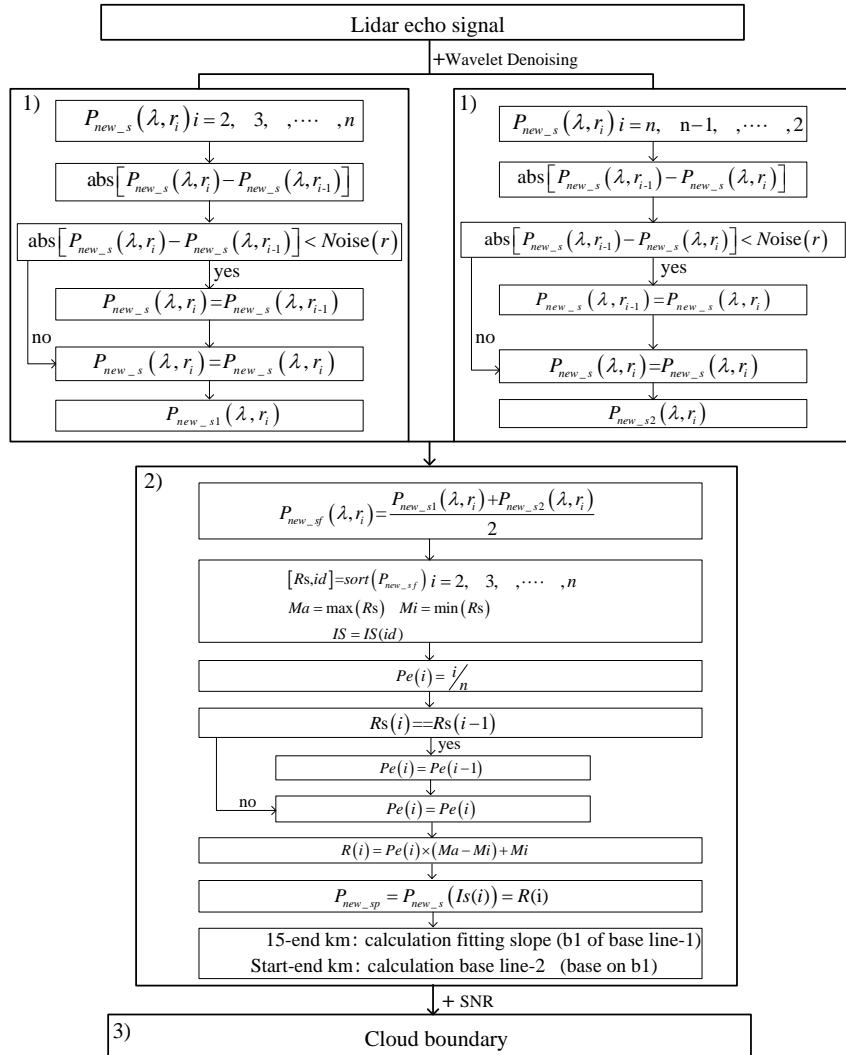
$$140 \quad \text{Noise}(r) = k \cdot Sd. \quad (5)$$

141 After the statistical analysis of the system noise, we set $k = 4$ in this study. The algorithm flow chart of detecting
 142 cloud boundary by lidar is shown in Fig. 2. Usually, the moving average of $P_{new}(\lambda, r)$ of lidar echo signal is
 143 calculated to reduce the influence of random noise. However, the selection of a sliding window directly affects the
 144 signal quality. Therefore, $P_{new}(\lambda, r)$ is denoised by wavelet transform, threshold function is a soft threshold, wavelet
 145 base is sym7, and the number of decomposition layers is 5. Using wavelet function to reduce noise can avoid too
 146 much smoothing remove sharp signal changes due to clouds, and can also avoid the improper selection of moving
 147 average window. Obtaining cloud boundaries mainly includes three parts. The first part is signal preprocessing.
 148 $P_{new_s}(\lambda, r)$ after wavelet de-noising is discretized based on the estimates of noise, and get useful signals $P_{new_s1}(\lambda, r)$
 149 and $P_{new_s2}(\lambda, r)$. The second part is to enhance the signal to make the cloud signal sharper from the background
 150 noise and aerosol signal. Average signals $P_{new_s1}(\lambda, r)$ and $P_{new_s2}(\lambda, r)$ to obtain $P_{new_sf}(\lambda, r)$. Ascending arrangement
 151 are conducted for $P_{new_sf}(\lambda, r)$ and the new sequence R_S and the corresponding index id are recorded. The maximum
 152 and minimum R_S are denoted as Ma and Mi , respectively. By building a new mapping proportion coefficient $Pe(i)$,
 153 the enhanced signal $P_{new_sp}(\lambda, r)$ is obtained. Obtain slope of baseline 1, and obtain baseline 2 based on this slope.
 154 Signals exceeding baseline 2 are regarded as candidate cloud signals as shown in Fig. 3b) and Fig. 4b). The third
 155 part is to extract cloud signal and realize boundary detection by combining the SNR of echo signal. By fitting the
 156 echo signal slope in the height range of 15–20 km, the slope is used as the slope to distinguish the cloud and aerosol
 157 layers (as shown by the magenta line in Fig. 3b and Fig. 4b). Without considering the bottom echo signal (0–2 km),

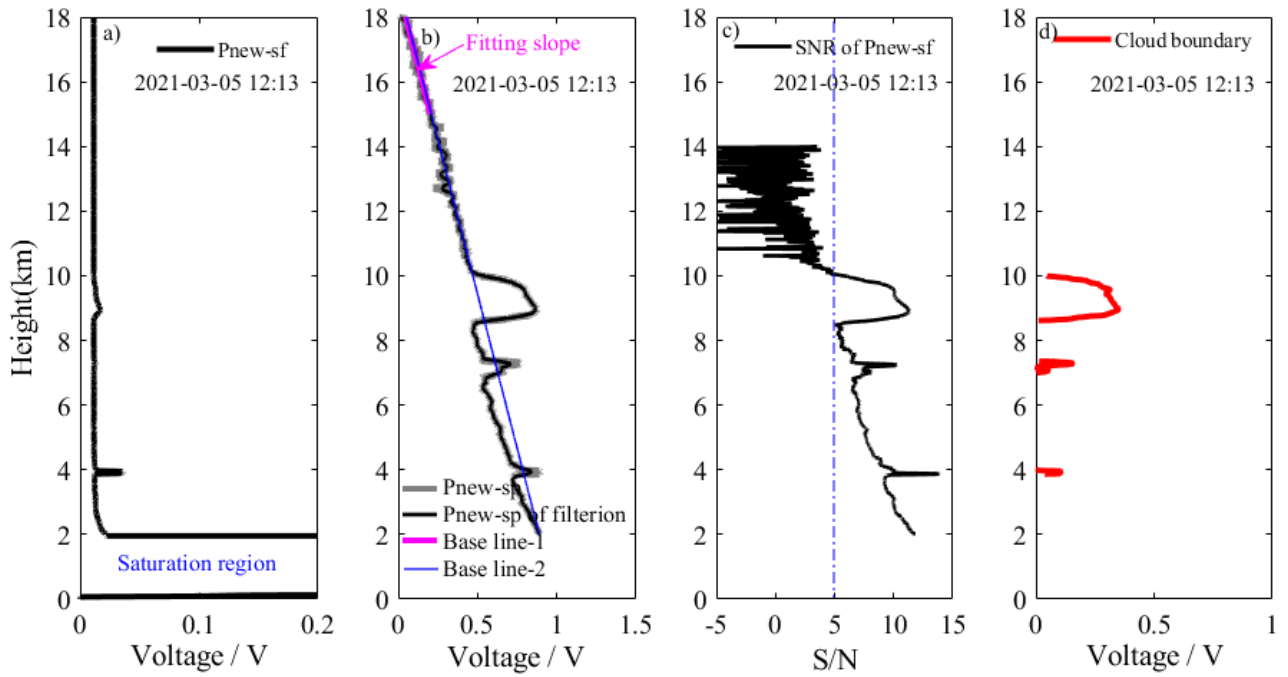
158 the amplitude of the echo signal received by the lidar decreased with increasing detection height according to the
 159 fitted slope, as shown by the blue line baseline in Figs. 3b) and 4b). When the beam senses the presence of clouds,
 160 the amplitude of the echo signal will exceed the blue baseline. The *SNR* of the echo signal is an important
 161 parameter for distinguishing the cloud and aerosol layers in the echo signal and calculating the *SNR* of P_{new_sf} using
 162 Eq. (6) (Xie et al., 2017),

$$163 \quad SNR(r, \lambda) = \frac{N \cdot P(r, \lambda)}{\sqrt{N \cdot P(r, \lambda) + N \cdot P_{back}}}, \quad (6)$$

164 where N is the pulse accumulation, and P_{back} is the solar background noise power. As shown in Figs. 3c) and 4c),
 165 the *SNR* of the cloud layer is higher than that of the aerosol layer and background noise, and the *SNR* in the cloud
 166 layer is approximately greater than 5 (obtained based on multidata statistical analysis in different situations).
 167 Combined with the *SNR* threshold, the detected cloud information is shown in Figs. 3d) and 4d). Compared with the
 168 traditional method of finding cloud bottom and cloud top from echo signals, this method first accurately extracts
 169 cloud signals, and then obtains cloud boundaries (cloud bottom and top). This method greatly reduces the
 170 interference caused by noise and aerosol signal.

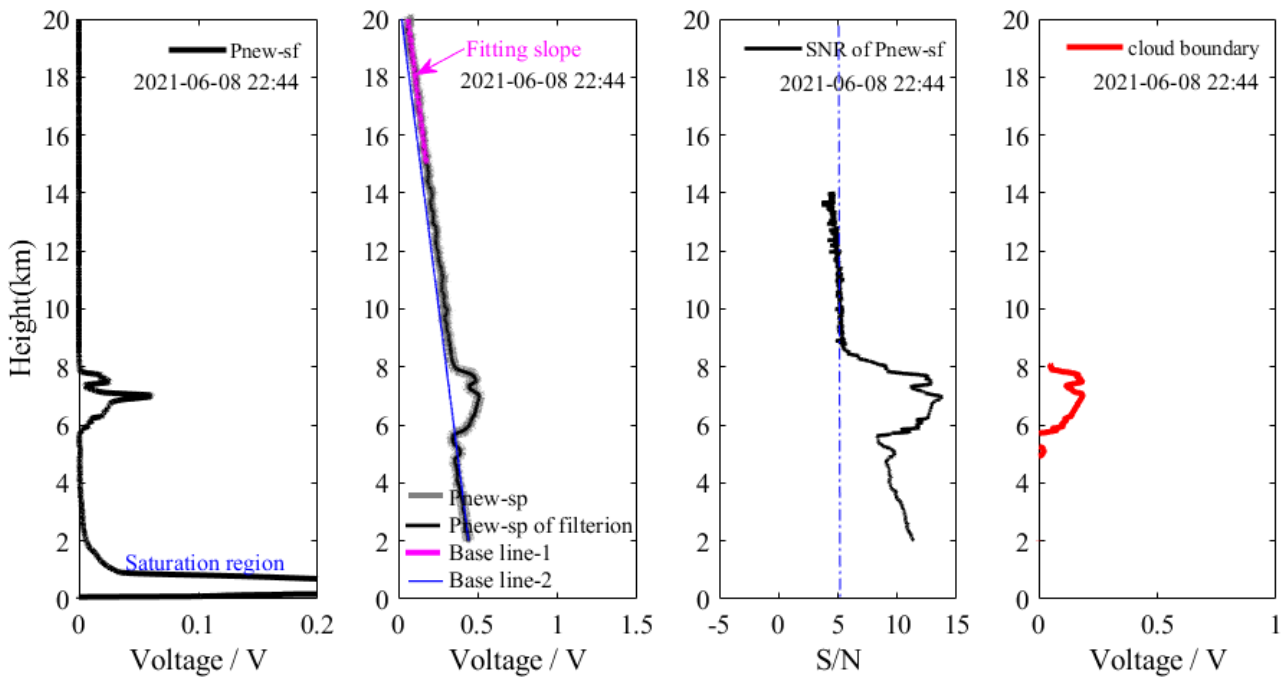


171
 172 Fig. 2 Use lidar to detect cloud boundary. 1) signal preprocessing, 2) baseline determination based on enhanced signal, 3) identifying
 173 cloud boundary with *SNR*



174
175
176

Fig. 3 Detection results of lidar at 12:13 on March 5, 2021. a) P_{new_sf} of the 1064 nm signal, b) P_{new_sp} of the 1064 nm signal, c) SNR of P_{new_sf} d) cloud information detected



177
178
179

Fig. 4 Detection results of lidar at 22:44 on June 8, 2021. a) P_{new_sf} of the 1064 nm signal, b) P_{new_sp} of the 1064 nm signal, c) SNR of P_{new_sf} d) cloud information detected

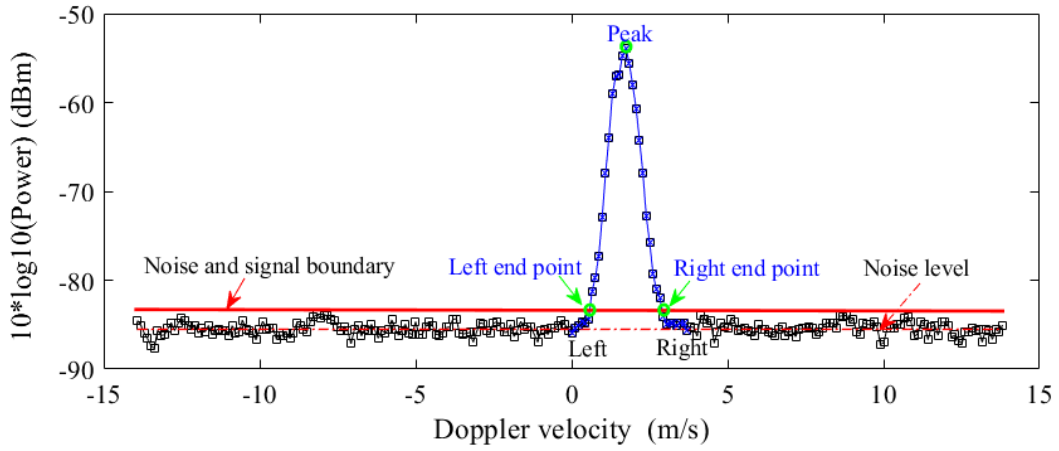
180 3.2 MMCR cloud boundary detection

181 Identifying cloud signals from Doppler spectra of the MMCR is affected by the noise level, particularly when the
 182 SNR is low. As shown in Fig. 5 (Di, H., et al., 2022), if all spectral points above the noise level are integrated, it will
 183 result in a large error in the inversion of its characteristic parameters (reflectivity factor, spectral width, radial
 184 velocity, etc.). Therefore, it is necessary to carefully identify cloud signals in Doppler spectra signal. There are two

185 parts in Fig. 6 includes two parts: recognition of cloud signals from Doppler spectra of MMCR and data quality
 186 control for MMCR. Part one is mainly to prepare for obtaining effective cloud signals. Generally, cloud signals
 187 have a certain number of continuous spectral points and SNR . With the part one of Fig. 6, we use the segmental
 188 method to calculate the noise level, and take it as the noise and signal boundary (as shown is Fig. 5). If spectral data
 189 amplitude is greater than SNR_{min} , and search for consecutive velocity bins in its spectral data and record the number
 190 of bins. When the number is larger than N_{ts} , and the corresponding spectral signals is determined as an effective
 191 spectrum segment. Intersections of effective spectral segment and noise and signal boundary are left and right
 192 endpoints of cloud spectral, that is, the starting and end point of the spectral moment calculation.

$$193 \quad SNR_{min} = \frac{25 \sqrt{N_F - 2.1325 + \frac{170}{N_P}}}{N_F \cdot N_P}, \quad (7)$$

194 where N_F is incoherent accumulation, and N_P is the number of fast fourier transform sampling points. The N_F and
 195 N_P of the MMCR used in this study are 32 and 256, respectively, and the SNR_{min} obtained by calculating the SNR_{min}
 196 is -17.74 dB. The SNR_{min} is adjusted according to the measured data of the MMCR and SNR_{min} is finally determined
 197 as -20 dB. Based on the research results of Shupe et al. (2008), N_{ts} is set to 7.



198
 199 Fig. 5 Schematic diagram of cloud signal recognition in Doppler spectra

200 The echo signals of floating debris in the low-level atmosphere have the characteristics of a small reflectivity factor,
 201 low velocity, and large spectral width. To further eliminate interfering wave information, we obtained the data
 202 quality control threshold by counting the characteristic changes in planktonic echoes in the boundary layer under
 203 cloud-free conditions. As shown in 2) of Fig. 6, when the reflectivity factor $Z < -20$ dBZ, the absolute value of
 204 radial velocity < 0.2 m/s, and the velocity spectrum width > 0.3 m/s are used as the threshold of noncloud
 205 information in bin. If the characteristic parameters of each bin meet the threshold, and assign NaN to the
 206 corresponding bin in reflectivity factor. The echo signals of floating debris in reflectivity factor are eliminated by
 207 the method, and the quality-controlled for reflectivity factor is realised.

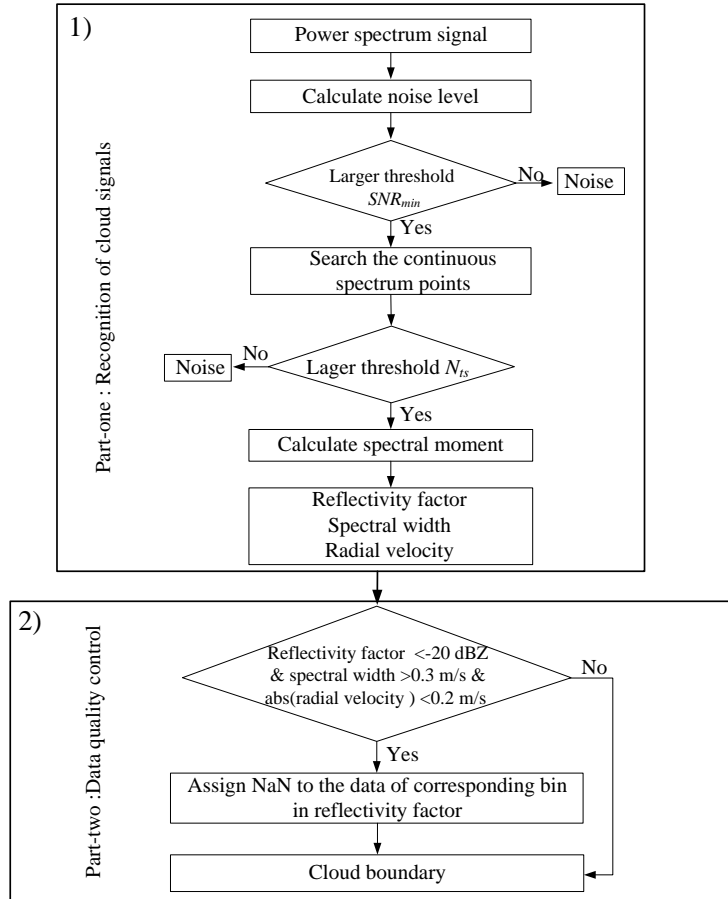


Fig. 6 Flow chart of MMCR cloud boundary detection. 1) recognition of cloud signals from Doppler spectra of MMCR, and 2) cloud boundary with data quality control

According to the algorithm flow in Fig. 6, Doppler spectra data at 22:44:00 on 8 June 2021 are analysed to obtain the cloud signals of the MMCR reflectivity factor, radial velocity, and velocity spectrum width, as shown in Fig. 7a)–c). The noncloud signals at the bottom (0–2 km) are effectively eliminated using the quality control algorithm shown in Fig. 6b). As shown in Fig. 7d) accurate recognition of cloud boundary is realized.

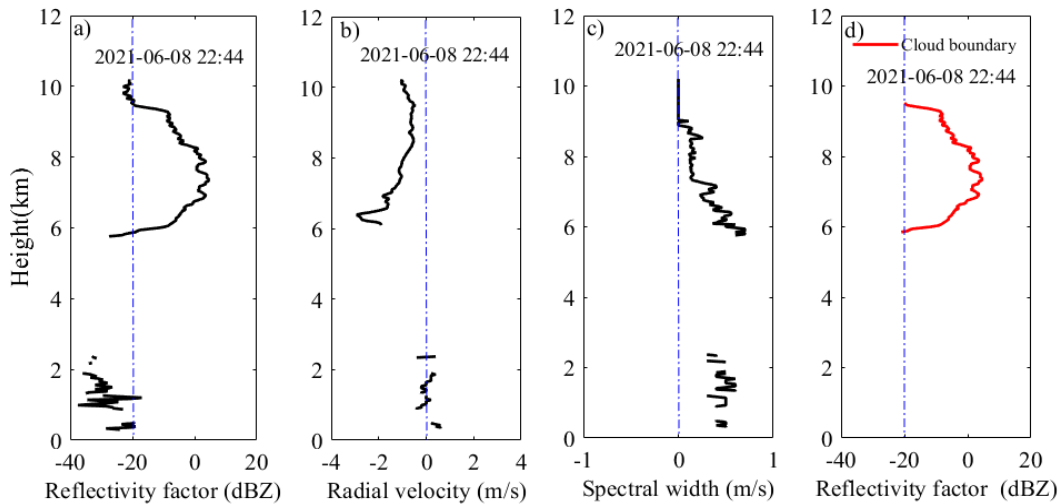


Fig. 7 Meteorological signals of MMCR at 22:44 on 8 June 2021. a) reflectivity factor, b) radial velocity, c) velocity spectrum width, d) reflectivity factor after quality control

218 **4 Results and discussion**

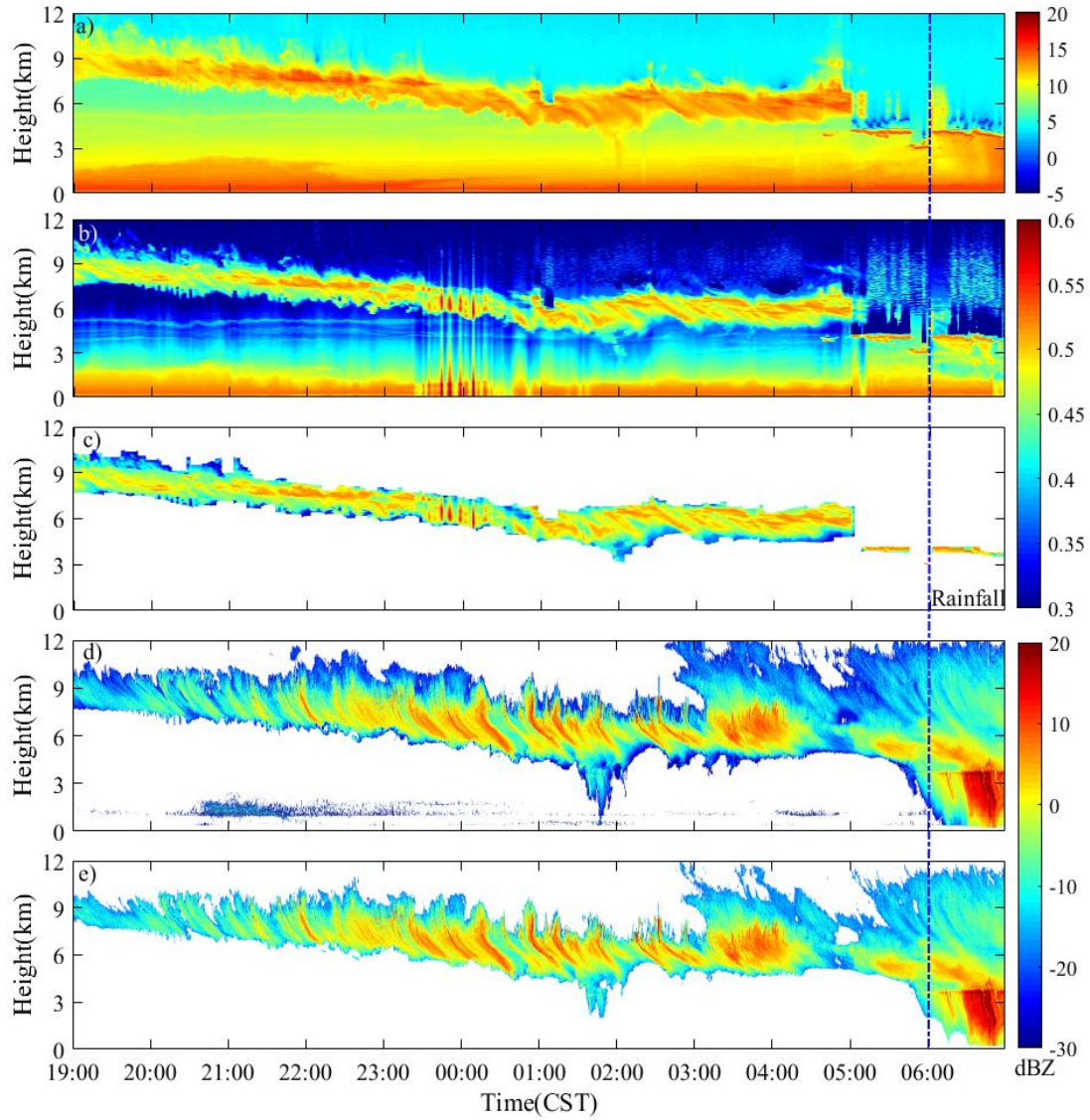
219 **4.1 Joint observation and analysis of various types of clouds**

220 Clouds change rapidly (Veselovskii et al., 2017). They often appear in the form of single-layer, multilayer, and
221 precipitating clouds. Section 4 uses the data inversion method proposed in Section 3 to analyse the changing
222 characteristics of clouds under different conditions to obtain reliable cloud macroinformation. Although the spatial
223 and temporal resolutions of the two detection devices are different, their close proximity allows a good
224 ‘point-to-point’ quantitative comparison between lidar and MMCR. Before data comparison and analysis, the low
225 spatial resolution of MMCR and low temporal resolution of the lidar were interpolated to keep the spatial and
226 temporal resolutions of the two consistent (the time resolution is 5 s, and the spatial resolution is 3.75 m).

227 1) First case study period

228 Clouds in the sky often appear as single-layer clouds and the inversion of macroscopic parameters is simpler than
229 that of multilayer clouds. June 08-09, 2021 (19:00–06:00 CST (China standard time)), lidar and MMCR jointly
230 monitored the appearance of monolayer clouds in Xi'an. According to the data method described in Section 3.1, we
231 can obtain cloud change information of time-height-indicator (THI) for SNR of P_{new_sf} and P_{new_sp} of lidar
232 @1064nm with a duration of 7 hours, as shown in Figs. 8a) and 8b). The inversion results show that the thickness
233 of the cloud layer is approximately 2 km, and the height of the cloud bottom decreases from 8 km to 4 km with the
234 passage of the observation time. After 05:00 CST, the cloud layer developed deeper, and the laser beam penetrated
235 0.1 km into the cloud layer and was quickly attenuated. Rainfall begins at 06:00 CST, and the lidar cannot continue
236 effective observation, and the experiment ends. The SNR in Fig. 8a) causes the SNR of the bottom signal to be large
237 (0–2 km, and the echo signal within the range is not considered in the following cases). Cloud signals have a higher
238 SNR than aerosols and background noise. P_{new_sp} highlights the cloud information from the aerosol signal and
239 background noise, and the details of the instability of the laser energy from 23:00 to 00:30 CST are displayed in Fig.
240 8b). Combined with the SNR ($SNR > 5.2$ without considering the low-level saturation zone) and P_{new_sp} thresholds
241 of the cloud signal in Fig. 8a) and 8b), the cloud layer signal detected from the echo signal is shown in Fig. 8c).

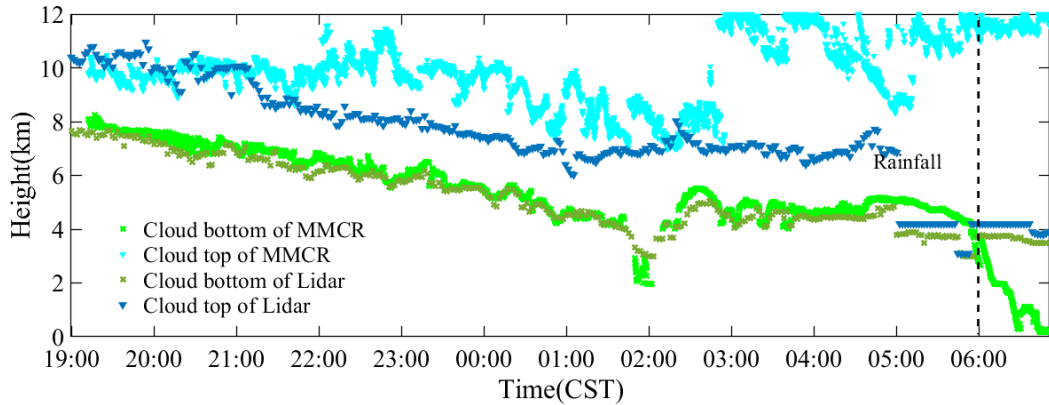
242 Cloud reflectivity factor of the MMCR for the same observation time period, and the cloud signals observed by the
243 two devices have good macrostructural similarity before 06:00 CST. As shown in Fig. 8d), when the quality control
244 of reflectivity factor is not conducted, noncloud signals in the range of 0–2 km are not prominent, and there are
245 some interference signals around the cloud. If we directly detect the cloud boundary with reflectivity factor in Fig.
246 8a), it will inevitably lead to underestimation or overestimation of the cloud boundary. We can effectively eliminate
247 the noncloud signals at the bottom atmosphere and the interference signals around the clouds using data quality
248 control for the reflectivity factor in Fig. 8e). According to the reflectivity factor of the MMCR, from 03:00 CST to
249 the end of observation, the cloud layer developed deeper, the cloud bottom height gradually decreased from 7 km to
250 300 m, and the cloud top height developed to ~12 km (the lidar signal fails to show this detail). When rain appeared
251 at 06:00 CST (The microwave radiometer accurately records the rainfall time, similar to the following), MMCR
252 cannot accurately detect the cloud bottom height, but lidar could detect it effectively (the cloud bottom boundary
253 was ~3.8 km). In this case, we can apply lidar and MMCR to detect cloud bottom and top boundaries, respectively,
254 to achieve high-precision detection of cloud boundaries.



255
 256 Fig. 8 THI of the echo signal of the lidar @1064 nm from 08 to 09 June 2021. a) SNR of P_{new_sf} , b) P_{new_sp} of the 1064 nm signal, c)
 257 cloud information detection results from lidar, d) reflectivity factor without quality control, e) reflectivity factor with quality control
 258 (black dotted line indicates rainfall time)

259 The cloud boundary is retrieved from the cloud signals detected by lidar and MMCR (Fig. 8c and Fig. 8e), and the
 260 results are shown in Fig. 9. Between 19:00 and 05:00 CST, the cloud bottom boundary height distributions retrieved
 261 by the two instruments were in agreement. Between 21:00 and 06:00 CST, with the development of clouds, the
 262 MMCR can detect more cloud information than lidar, especially from 03:00 to 06:00 CST. Although lidar cannot
 263 penetrate more clouds during this period, it can provide an effective cloud bottom boundary. At 19:00–20:00 CST,
 264 in cloud top boundaries where the ice crystals are too small to be detected by the MMCR, lidar detects the real
 265 cloud top. This is attributable to the echo intensity of the MMCR being proportional to the 6th power of the particle
 266 diameter, and the lidar echo signal is proportional to the square of the particles. From 19:00 to 00:00 CST, cirrus
 267 cloud transition to altostratus, where size of cloud particles increases in the form of collision and finally produces

268 precipitation. In this process, the lidar beam entering the cloud is attenuated, but MMCR has a good advantage in
269 cloud-top detection.

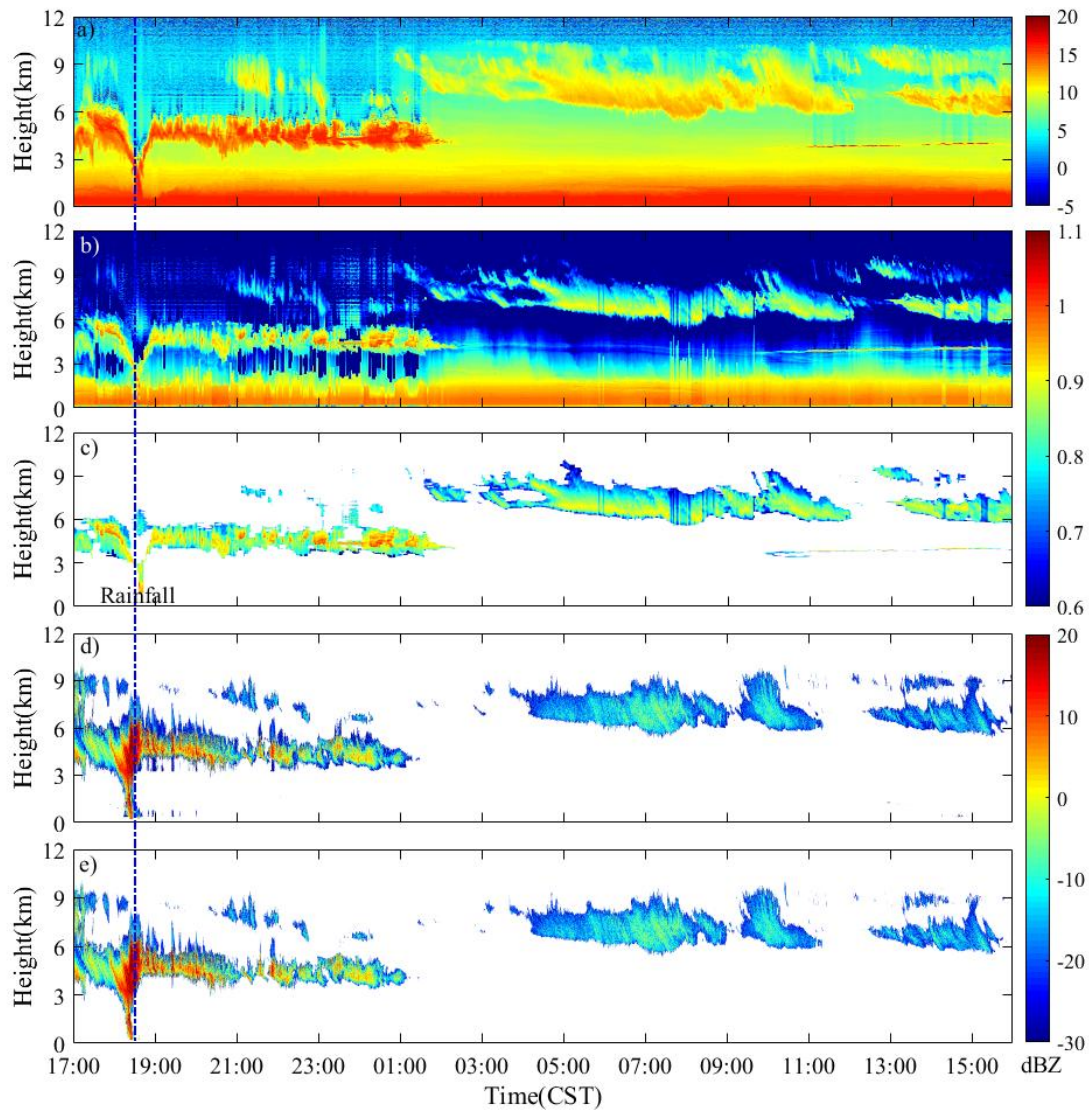


270
271

Fig. 9 Cloud boundary detected by lidar and MMCR from 8 to 9 June, 2021

272 2) Second case study period

273 From 4 to 5 March 2021, the MMCR and lidar conducted joint observations with a total observation time of 23 h.
274 By inverting the echo signal of the lidar @1064 nm, we obtained P_{new_sp} of the echo signal and the SNR of P_{new_sf} ,
275 and the plotted THIs are shown in Figs. 10a) and 10b). These THIs reveal that the double layers of the clouds
276 appeared in the sky during the observation period. The low-level cloud is located at a height of 4 km, and its
277 thickness is approximately 2 km; the high-level cloud lies at 7 km, and its thickness is ~ 2.7 km. The SNR of the
278 low-level cloud was significantly stronger than that of the high-level cloud, as shown in Fig. 10a). From the
279 characteristic distribution of the P_{new_sp} signal in Fig. 10b), the low-level cloud rained from 18:30 to 18:45 CST, and
280 the cloud bottom height decreased sharply from 4 km to 0.6 km. Subsequently, the cloud layer gradually dissipated
281 from 2 km to 0.05 km, and the dispersal that occurred from 02:00 to 10:00 CST was too strong for the lidar to
282 detect more detailed information about the low-altitude cloud. We also observed the high-level cloud change
283 characteristics shown in Fig. 10b). From 17:00 to 01:00 CST, there was a relatively weak P_{new_sp} signal in the height
284 range between 7 km and 10 km. This indicates that the high-level cloud may be in the formation stage at this time,
285 and the particle diameter and number concentration of clouds are so small that lidar can only receive a very weak
286 echo signal. As the observations progressed, the development of high-level clouds became relatively mature, and
287 the structure was relatively stable from 01:00 to 15:00 CST (except at 13:00 CST). Combined with the thresholds of
288 the SNR and intensity information of the cloud signal in Fig. 10a) and 10b), complete cloud signal detection can be
289 realised, as shown in Fig. 10c).

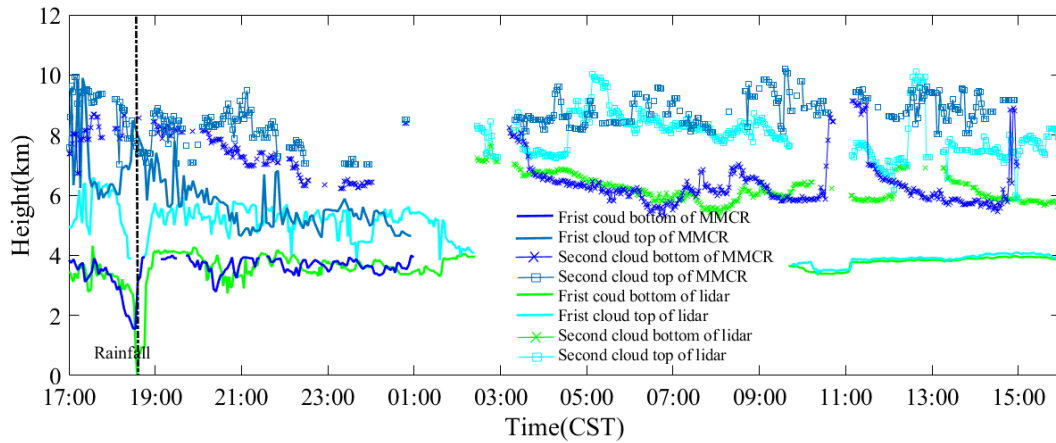


290
 291 Fig. 10 THI of the echo signal of the lidar @1064 nm from 4 to 5 March, 2021. a) SNR of P_{new_sf} , b) P_{new_sp} of the 1064 nm signal, c)
 292 cloud information detection results, d) reflectivity factor without quality control, e) reflectivity factor with quality control (black dotted
 293 line indicates rainfall time)

294 During lidar observations, the MMCR also observed double clouds. Figs. 10d) and 10e) show the signal
 295 distribution characteristics of the reflectivity factor of the MMCR without quality control and after quality control,
 296 respectively. It can be seen in Fig. 10e) that after data quality control, the noncloud signals and interference signals
 297 at the bottom are effectively eliminated. The joint observation results of the lidar and MMCR reveal that the
 298 appearance and shape of clouds observed by the two are similar, and the occurrence of rainfall was monitored from
 299 18:30 to 18:45 CST. From 17:00 to 01:00 CST, the penetration ability of the MMCR was markedly better than that
 300 of the lidar, and more high-level cloud information was obtained. However, between 01:00 and 04:00 CST for
 301 high-level clouds (approximately 8 km), the MMCR detected only part of the debris cloud echo signal, whereas the
 302 lidar detected more cloud information. We can speculate that the main reason for this is that clouds were in the
 303 growth stage during this time period, their particle diameters were small, or their concentrations were low. The echo
 304 signal of the MMCR is proportional to the 6th power of the particle diameter, whereas the echo signal of the lidar is
 305 proportional to the 2nd power of the particle diameter; therefore, the lidar can detect clouds that the MMCR cannot

306 detect. From 10:00 to 15:00 CST, the MMCR also failed to detect the thin cloud signal in the lower layer (a height
 307 of approximately 4 km). Another reason for MMCR failing to detect thin clouds may be that its spatial resolution is
 308 lower than that of lidar, which makes it unable to detect thin clouds.

309 The height distribution of the double-layer cloud boundaries was detected based on the cloud signals (Fig. 10c and
 310 Fig. 10e) jointly observed by lidar and MMCR, as shown in Fig. 11. The cloud boundary height distribution shows
 311 that the cloud boundary height distributions detected by lidar and MMCR are relatively consistent for low-level
 312 clouds. For high-level clouds, the heights of the cloud bottom boundary detected by the two instruments were
 313 similar, and the cloud top boundary detected by MMCR was higher than that detected by lidar. However, compared
 314 with MMCR, lidar is superior in detecting thin cloud information.



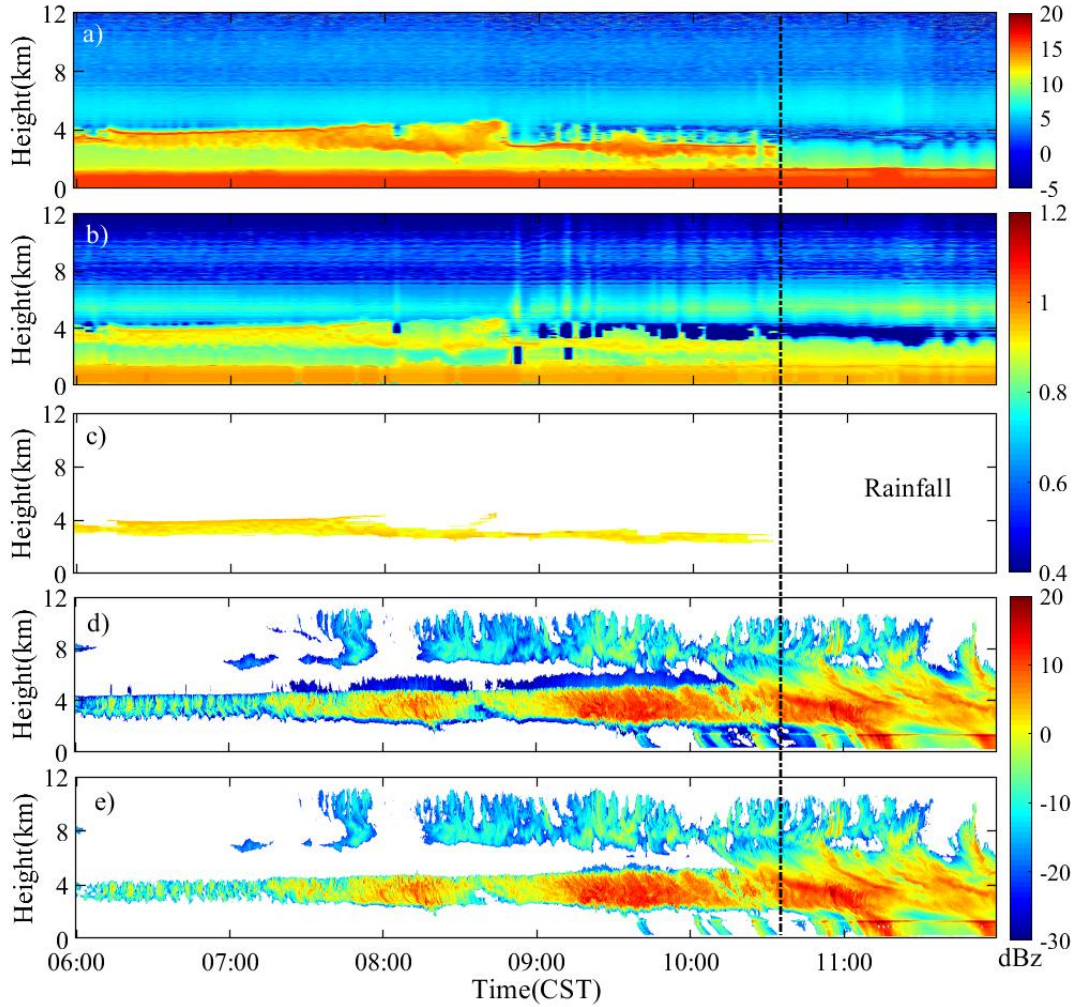
315
 316 Fig. 11 Cloud boundary detected by the lidar and MMCR from 4 March to 5, 2021

317 3) Third case study period

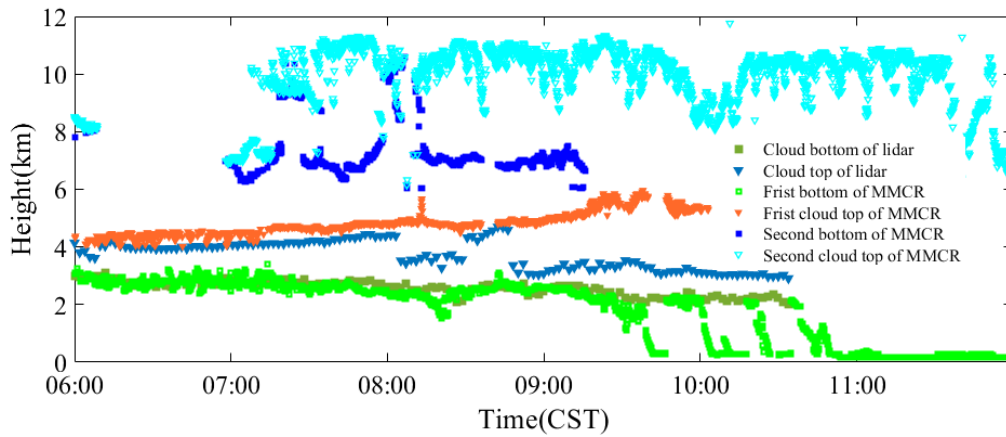
318 On 10 March 2021 lidar and MMCR jointly observed clouds before rainfall for 6 h (06:00–11:00 CST, and began to
 319 rain at 10:45 CST). Fig. 12a) shows the distribution of the SNR of P_{new_sf} with time and space, Fig. 12b) shows the
 320 THI of P_{new_sp} of the @1064 nm echo signal, and Fig. 12c) shows the cloud signal detected by the thresholds of the
 321 SNR and P_{new_sp} . We inverted the reflectivity factor of the MMCR and performed data quality control operations on
 322 them. The results are shown in Fig. 12d) and Fig. 12e), which are the reflectivity factor of the MMCR without
 323 quality control and quality control, respectively. From the comparison, it is evident that data quality control can
 324 eliminate the interference signal very well, which simplifies the process of merging the high-level convective cloud
 325 and the low-level stratiform cloud.

326 By comparing the cloud information detected by the lidar and MMCR (Fig. 12c and Fig. 12e), we can see that
 327 during the period from 06:00 to 10:00 CST, the energy of the lidar beam is severely attenuated at a height of
 328 approximately 4 km, resulting in a very weak echo signal and SNR above 4 km. As the observation time progressed,
 329 the phenomenon of virga (> -15 dBZ) occurred in the cloud (Ellis et al., 2011; Williams et al., 2014). The severe
 330 attenuation of lidar in the cloud leads to a sharp decrease in its detection ability, whereas the millimeter wave still
 331 has a strong penetrating ability. When rainfall occurs (at 10:45 CST), neither lidar nor MMCR can effectively
 332 identify the cloud bottom boundary, but MMCR can still detect cloud top boundary information. The height
 333 distributions of the cloud boundaries detected by lidar and MMCR are shown in Fig. 13. The height distribution of
 334 the cloud bottom and cloud top boundaries detected by the two instruments is almost the same from 06:00 to 09:00

335 CST (the cloud bottom boundary is approximately 3 km, and the cloud top boundary is approximately 4.1 km). A
 336 drizzle fell from 09:00 to 10:45 CST, and the lidar obtained an effective cloud bottom boundary. The boundary of the
 337 the high-level convective cloud at ~8 km and the deep cloud layer from 10:45 CST to the end of the observation
 338 period can only be detected by MMCR.



339
 340 Fig. 12 THI of echo signal of the lidar and MMCR on 10 March, 2021. a) SNR of P_{new_sf} , b) P_{new_sp} of the 1064 nm signal, c) cloud
 341 information detection results, d) reflectivity factor without quality control, e) reflectivity factor with quality control (black dotted line
 342 indicates rainfall time)

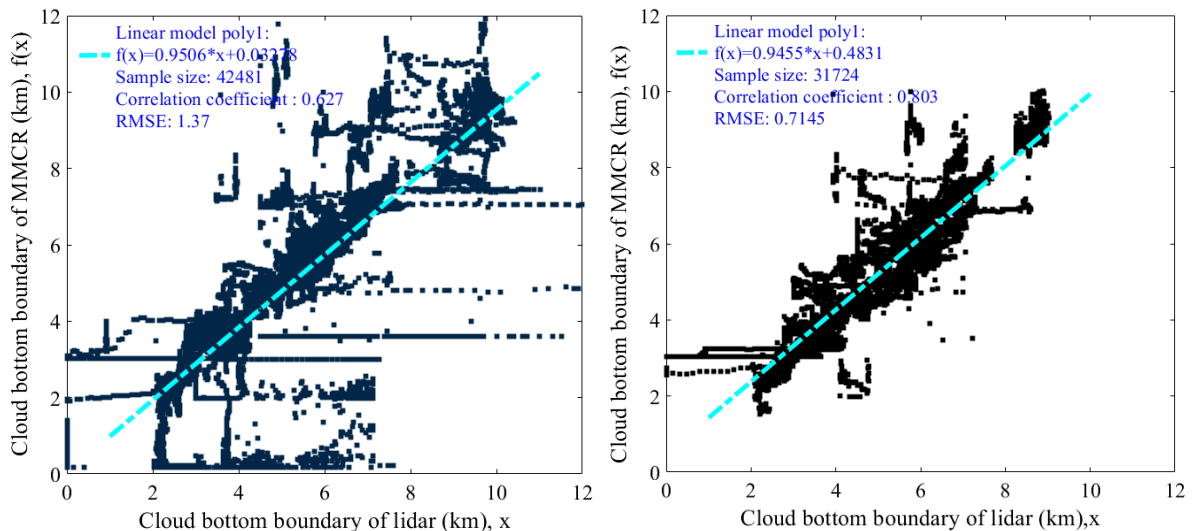


343
 344 Fig. 13 Cloud boundary detected by the lidar and MMCR on 10 March, 2021

345 From the differences in the height distribution of the cloud boundaries reached by the two devices in the above
 346 three different situations, it can be seen that when a single layer of stratiform clouds appears in the sky, the heights
 347 of the cloud bottom boundary detected by the MMCR and lidar are approximately the same. When there are
 348 multilayer clouds, MMCR and lidar have good consistency in the detection results of the cloud bottom boundary
 349 height of the low-level cloud; however, the energy of the lidar beam attenuates significantly in the low-level cloud,
 350 resulting in an inability to fully obtain the effective bottom boundary of low-level clouds and the height boundary
 351 of high-level clouds. In this case, the MMCR can obtain more complete height information for the multilayer cloud
 352 boundary. Usually, the closer rainfall is, the deeper the cloud layer develops, **the more severely the beam of the**
 353 **lidar will be attenuated**, and more cloud information cannot be obtained. In other words, MMCR still has the ability
 354 to penetrate the cloud layer and detect **complete cloud information**. Therefore, the joint observation of lidar and
 355 MMCR can comprehensively identify and detect cloud boundary conditions in detail. The difference between the
 356 cloud boundaries detected by the two may also be due to the different scattering mechanisms of cloud particles to
 357 millimeter-wave electromagnetic waves and laser beams or the difference in the methods used by the two devices
 358 to determine the cloud boundary; thus, there are some differences in the cloud boundary height results.

359 **4.2 Analysis of cloud boundary distribution characteristics in Xi'an**

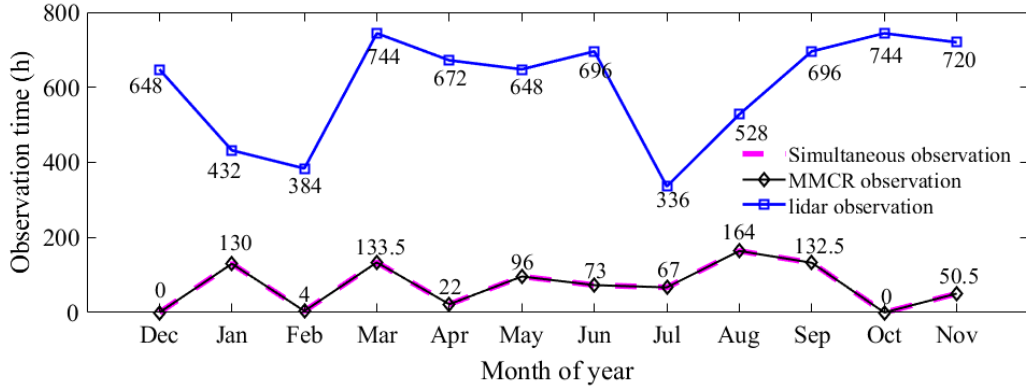
360 **To further analyse the changes in the height distribution of cloud boundaries in Xi'an, we plan to use MMCR and**
 361 **lidar data for cloud boundary analysis.** Accordingly, it is necessary to analyse the correlation of the cloud bottom
 362 boundary height detected by the two devices. We randomly selected 80 h of data in the joint observation period (to
 363 avoid the rainfall period) and calculated the cloud boundary detection results of lidar and MMCR according to the
 364 data processing methods in Sections 3.1 and 3.2. As shown in Fig. 14, when the quality control of the MMCR is
 365 performed, the correlation between the detected cloud boundary and lidar detection result increases from 0.627 (in
 366 Fig. 14a) to 0.803 (in Fig. 14b)). Moreover, under the premise that the difference in cloud boundaries caused by
 367 the different detection **principles and algorithms** of the two devices cannot be avoided, we can use the cloud
 368 boundary data detected by MMCR to replace the missing lidar data.



369
 370 Fig. 14 Correlation between lidar and MMCR cloud bottom. a) without quality control; b) with quality control

371 From the above three cloud observation cases, it can be seen that MMCR has more advantages than lidar in
 372 detecting cloud-top boundaries. Therefore, when calculating the cloud boundary height distribution characteristics
 373 over Xi'an, we only counted the cloud top boundary height detected by the MMCR and considered it as the actual

374 cloud top boundary. From December 2020 to November 2021, MMCR and lidar stored 302 d (7248 h) and 126 d
 375 (872.5 h) of observational data, respectively. During the 12-month observation period, the maximum detection
 376 altitude of the MMCR changed. From December 2020 to June 2021, the maximum detection range of MMCR is
 377 12.6 km, and the maximum detection height is changed to 18 km. The total observation hours of MMCR and lidar
 378 for each month are shown in Fig. 15. The hours of lidar, MMCR, and simultaneous measurements are 872.5 h. In
 379 this study, the four seasons were defined as follows: spring from March to May (MAM), summer from June to
 380 August (JJA), autumn from September to November (SON), and winter from December to February (DJF).



381
382 Fig. 15 Monthly observation hours of lidar and MMCR

383 Table 3 establishes the rules for recording effective cloud bottom information in the observation process using
 384 MMCR and lidar under different conditions to improve the detection accuracy of the cloud-bottom boundary.

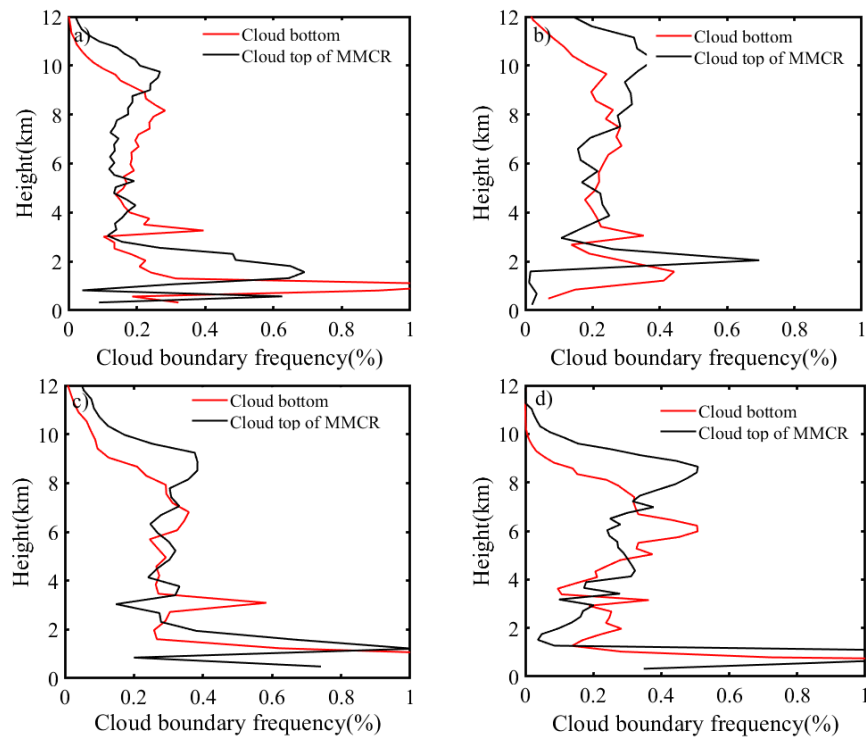
385 Table 3 Cloud bottom height recording guideline

Detection equipment	Observation	Detection conditions	Record cloud bottom boundary
Both the lidar and MMCR	Case 1	Geometrical thin cloud: the lidar detects bottom; MMCR did not detect the cloud bottom	Results of the lidar
	Case 2	Drizzle: the lidar detects bottom; bottom of MMCR is invalid	Results of the lidar
	Case 3	Both the lidar and MMCR detect cloud bottom	Record the lower value of the cloud bottom boundary
MMCR	Case 4	MMCR detected cloud bottom	Results of MMCR
	Case 5	Drizzle: bottom of MMCR is invalid	No results are recorded

386 This study defines ‘cloud occurrence frequency’ as the ratio of cloud occurrence times to total detection times
 387 during the analysed period. The total sample size is N , and the sample size of cloud boundaries appearing at
 388 different height levels (altitude range from 1.5 km to 12 km is divided into 50 levels) is n_i . The seasonal distribution
 389 characteristics of the cloud boundary height are calculated according to Eq. (8),

390
$$y_{cloud} = \frac{n_i}{N} (n_i \in N, i = 1, \dots, 50). \quad (8)$$

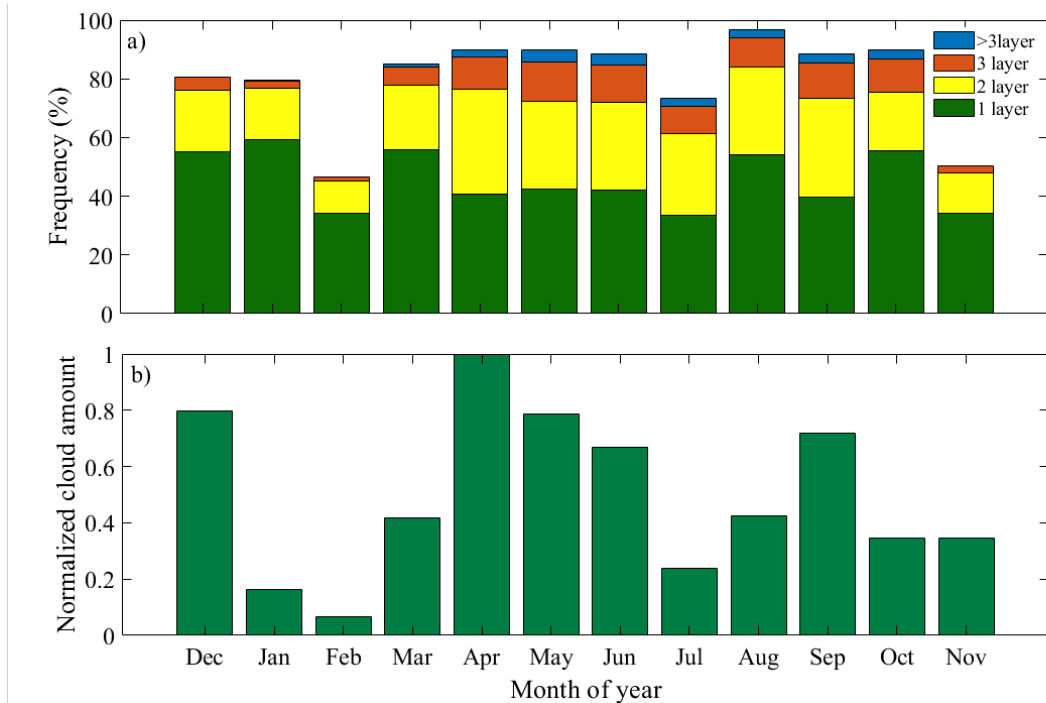
391 Fig. 16 shows the vertical frequency distribution of the cloud boundary seasonally from December 2020 to
 392 November 2021. For the vertical distribution of cloud base, the first narrow peaks is the boundary layer clouds (\leq
 393 1.5 km), the second peak is 2.5–3.5 km, and the third peak has a big range in vertical height, which is 4.7–10 km a
 394 in spring. Fig.16 (b) shows that the cloud bottom height in summer is mainly distributed at 3–9.5 km, indicating
 395 that middle and high clouds may be dominant. The distribution of cloud bottom is bimodal, the first peak is the
 396 boundary layer cloud peak, and the second peak is located at 2.7–3.7 km and 3.6–8.3 km in autumn and winter,
 397 respectively. The variation in cloud top with seasons shows a bimodal distribution, and spring and summer have a
 398 similar trend of cloud top boundary height distribution. The frequency of the cloud top boundary above 10 km was
 399 the highest, and the frequency below 2 km was the lowest in summer. The distribution characteristics of cloud top
 400 height in autumn and winter indicate that the frequency of low clouds is higher than that in the other two seasons.
 401 This is consistent with the results of Zhao et al. (2014) for the SGP site and Hailing Xie (2017) for the SACOL site.
 402 Although there were some differences in the cloud boundary frequency distribution at some heights, the overall
 403 change trend was roughly the same.



404
 405 Fig. 16 Frequency distribution of cloud boundaries during (a) spring, (b) summer, (c) autumn, and (d) winter from December 2020 to
 406 November 2021 at Xi'an Jinghe National Meteorological Station

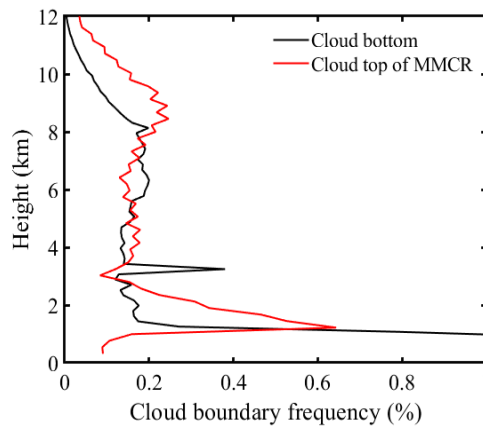
407 Fig. 17 a) shows the monthly variation frequency distribution of clouds. The months with the largest and smallest
 408 cloud occurrence frequencies are August and February, respectively. Almost more than 34% of the clouds appear in
 409 the form of single layer clouds every month. Compared with January, February, November, and December, the
 410 frequencies of double-layer clouds, triple-layer clouds, and more clouds in other months are higher. To show the
 411 relative change trend of cloud cover, we calculated the total cloud cover of each month by using the total cloud
 412 cover at each time stored by the MMCR. It was found that the maximum cloud cover was in April. Therefore, the

413 total cover of April was set to 1, and the normalized cloud cover distribution of 12 months was obtained, as shown
 414 in the Fig. 17 b). It can be seen from the distribution of cloud cover in every month that the cloud cover is high in
 415 summer and the least in winter, indicating that warm atmospheric conditions are more conducive to the formation
 416 and development of clouds.



417
 418 Fig. 17 Monthly variation in cloud frequency distribution and cloud cover from December 2020 to November 2021 a) monthly
 419 variation in the frequency of the number of cloud layers. b) monthly variation in cloud cover

420 As Fig.18 caption says it is the frequency distribution of cloud boundaries observed over Xi'an from December
 421 2020 to November 2021. Frequency of the cloud bottom boundary below the vertical height of 1.5 km is the highest,
 422 the frequency within the height range of 3.06 km and 3.6 km is approximately 0.4%, and the frequency above 8 km
 423 is less than 0.2%. The frequency of the cloud top boundary at vertical heights has a bimodal distribution, and the
 424 first narrow peak is located at 1.0–3.1 km, and the second peak lies at 6.4–10.5 km. Combined with the changing
 425 characteristics of cloud layers, it can be seen that during observation in Xi'an, the frequency of clouds below 3.5 km
 426 is the largest, and the frequency of high-level ice clouds or cirrus clouds above 8 km is small.



427
 428 Fig. 18 Frequency distribution of cloud boundaries at vertical heights at Xi'an Jinghe National Meteorological Station from December
 429 2020 to November 2021

430 **5 Conclusions**

431 Based on the observation data of lidar, a new algorithm is proposed which can effectively extract cloud signals.
432 Compared with the previous method of identifying cloud bottom and cloud top from echo signals, the new method
433 mainly obtains effective cloud signals through suppressing noise signals and enhancing effective signals to realize
434 cloud boundaries. The algorithm has two main characteristics: 1) in the signal preprocessing, wavelet transform is
435 used for the original signal to avoid the defect of effective information loss caused by improper selection of smooth
436 window; 2) The SNR of the signal is considered.

437 The cloud signals in Doppler spectra are effectively extracted by analyzing the noise level, SNR_{min} , and the
438 continuous spectral points of Doppler spectra. The data quality control conditions for MMCR (reflectivity factor <
439 -20 dBZ, spectrum width > 0.3 m/s and radial velocity < 0.2 m/s) were established by analyzing the characteristic
440 of the interference of floating debris signals. By analysing the correlation of cloud bottom height between MMCR
441 and lidar, and the cloud bottom height detection by MMCR with data quality control have a good agreement with
442 lidar (the correlation coefficient is 0.803). Therefore, quality control is an important factor to improve signal
443 accuracy of MMCR.

444 In this study, combined with the respective advantages of MMCR and lidar in cloud detection, the cloud cover and
445 distribution of cloud boundaries characteristics are analyzed based on the observation data in Xi'an from December
446 2020 to November 2021. The result reveals that more than 34% of the clouds appear in the form of a single layer
447 every month. The cloud cover was lowest in spring and highest in summer. The seasonal variation in cloud
448 boundary height showed that the distribution characteristics of cloud boundaries in spring and summer were similar,
449 and the frequency of high-level clouds in the range of 8–10 km was greater than autumn and winter. The stratiform
450 clouds appearing below 3.5 km in autumn have the highest frequency, and high-level ice clouds or cirrus clouds
451 above 8 km in winter are less likely to appear. The findings can provide a preliminary analysis of cloud boundary
452 changes in Xi'an. If there are huge amounts of simultaneous observation data of the lidar and MMCR, the
453 comprehensive statistics and analysis of cloud macro and micro parameters in Xi'an can be realized, which can
454 provide better support for the study of climate change characteristics in Xi'an.

455 **Data availability**

456 The data and code related to this article are available upon request from the corresponding author.

457 **Author contributions**

458 Conceptualization: Yun Yuan

459 Investigation: Yun Yuan

460 Methodology: Yun Yuan and Huige Di

461 Software: Yun Yuan

462 Supervision: Huige Di and Dengxin Hua

463 Methodology and software improvement: Yuanyuan Liu, Tao Yang, Qimeng Li, Qing Yan, Wenhui Xin, and
464 Shichun Li.

465 Writing – original draft: Yun Yuan

466 Writing – review & editing: Yun Yuan and Huige Di

467 [Project administration: Dengxin Hua](#)

468 **Competing interests**

469 The authors declare that they have no conflicts of interest related to this work.

470 **Financial support**

471 This research has been supported by the National Natural Science Foundation of China, Innovative Research Group
472 Project of the National Natural Science Foundation of China (grant nos. 42130612, 41627807 and [61875162](#)) and
473 [the Ph.D. Innovation fund projects of Xi'an University of Technology \(Fund No.310-252072106\)](#).

474 **References**

- 475 Apituley, A., van, Lammeren, A., and Russchenberg, H.: High time resolution cloud measurements with lidar
476 during CLARA, *Phys. Chem. Earth.*, 25(2), 107-113, [https://doi.org/10.1016/S1464-1909\(99\)00135-5](https://doi.org/10.1016/S1464-1909(99)00135-5), 2000.
- 477 [Borg, L. A., Holz, R. E., and Turner, D. D.: Investigating cloud radar sensitivity to optically thin cirrus using
478 collocated Raman lidar observations, *Geophys. Res. Lett.*, 38, L05807, <https://doi.org/10.1029/2010gl046365>,
479 2011.](#)
- 480 Cao, X., Lu, G., Li, M., and Wang, J.: Statistical Characteristics of Cloud Heights over Lanzhou, China from
481 Multiple Years of Micro-Pulse Lidar Observation, *Atmosphere.-Basel.*, 12(11), 1415,
482 <https://doi.org/10.3390/atmos12111415>, 2021.
- 483 Chen, Z., and Sun, X.: Dynamic spatial fusion of cloud top phase from PARASOL, CALIPSO, cloudsat satellite
484 data, *J. Quant. Spectrosc. Ra.*, 224, 176-184, <https://doi.org/10.1016/j.jqsrt.2018.11.010>, 2019.
- 485 Clothiaux, E. E., Moran, K. P., Martner, B. E., Ackerman, T. P., Mace, G. G., Uttal, T., Mather, J. H., Widener, K.
486 B., Miller, M. A., and Rodriguez, D. J.: The atmospheric radiation measurement program cloud radars:
487 Operational modes, *J. Atmos. Ocean. Tech.*, 16(7), 819-827,
488 [https://doi.org/10.1175/1520-0426\(1999\)016%3C0819:TARMPC%3E2.0.CO;2](https://doi.org/10.1175/1520-0426(1999)016%3C0819:TARMPC%3E2.0.CO;2), 1999.
- 489 Cordoba-Jabonero, C., Lopes, F. J. S., Landulfo, E., Cuevas, E., Ochoa, H., and Gil-Ojeda, M.: Diversity on
490 subtropical and polar cirrus clouds properties as derived from both ground-based lidars and CALIPSO/CALIOP
491 measurements, *Atmos. Res.*, 183, 151-165, <https://doi.org/10.1016/j.atmosres.2016.08.015>, 2017.
- 492 [Delanoe, J., and Hogan, R. J.: A variational scheme for retrieving ice cloud properties from combined radar, lidar,
493 and infrared radiometer, *J. Geophys. Res.-Atmos.*, 113, D07204, <https://doi.org/10.1029/2007jd009000>, 2008.](#)
- 494 [Di,H., Yuan,Y., Yan,Q., Xin,W., Li,S., Wang,J., Wang,Y., Zhang,L., and Hua, D.: Determination of atmospheric
495 column condensate using active and passive remote sensing technology, *Atmos. Meas. Tech.*, 15, 3555–3567,
496 <https://doi.org/10.5194/amt-15-3555-2022>, 2022.](#)
- 497 [Dong, X., Xi, B., Crosby, K., Long, C. N., Stone, R. S., and Shupe, M. D.: A 10 year climatology of Arctic cloud
498 fraction and radiative forcing at Barrow, Alaska, *J. Geophys. Res.*, 115, D17212,
499 <https://doi.org/10.1029/2009jd013489>, 2010.](#)
- 500 Ellis, S. M., and Vivekanandan, J.: Liquid water content estimates using simultaneous S and K a band radar
501 measurements, *Radio. Sci.*, 46(RS2021), 1-15, <https://doi.org/10.1029/2010RS004361>, 2011.
- 502 [Gürsdorf, U., Lehmann, V., Bauer-Pfundstein, M., Peters, G., Vavriv, D., Vinogradov, V., and Volkov, V.: A 35-GHz
503 polarimetric Doppler radar for long-term observations of cloud parameters—Description of system and data](#)

504 processing, *J. Atmos. Ocean. Tech.*, 32(4), 675-690, <https://doi.org/10.1175/JTECH-D-14-00066.1>, 2015.

505 Hobbs, P. V., Funk, N. T., Weiss, Sr. R. R., Lohn, J. D., and Biswas, K. R.: Evaluation of a 35 GHz radar for cloud
506 physics research, *J. Atmos. Ocean. Tech.*, 2(1), 35-48,
507 [https://doi.org/10.1175/1520-0426\(1985\)002<0035:EOAGRF>2.0.CO;2](https://doi.org/10.1175/1520-0426(1985)002<0035:EOAGRF>2.0.CO;2), 1985.

508 Intrieri, J. M., Stephens, G. L., Eberhard, W. L., and Uttal, T.: A method for determining cirrus cloud particle sizes
509 using lidar and radar backscatter technique, *J. Appl. Meteorol. Clim.*, 32(6), 1074-1082,
510 [https://doi.org/10.1175/1520-0450\(1993\)032%3C1074:AMFDCC%3E2.0.CO;2](https://doi.org/10.1175/1520-0450(1993)032%3C1074:AMFDCC%3E2.0.CO;2), 1993.

511 Kitova, N., Ivanova, K., Mikhalev, M. A., and Ausloos, M.: Statistical investigation of cloud base height time
512 evolution, *Proc. SPIE-Int. Soc. Opt. Eng.*, 5226, 280-284, <https://doi.org/10.1117/12.519500>, 2003.

513 Kollias, P., Clothiaux, E. E., Miller, M. A., Albrecht, B. A., Stephens, G. L., and Ackerman, T. P.:
514 Millimeter-wavelength radars: New frontier in atmospheric cloud and precipitation research, *B. Am. Meteorol.*
515 *Soc.*, 88(10), 1608-1624, <https://doi.org/10.1175/BAMS-88-10-1608>, 2007.

516 Kollias, P., Clothiaux, E. E., Miller, M. A., Luke, E. P., Johnson, K. L., Moran, K. P., Widener, K. B., and Albrecht,
517 B. A.: The Atmospheric Radiation Measurement Program cloud profiling radars: Second-generation sampling
518 strategies, processing, and cloud data products, *J. Atmos. Ocean. Tech.*, 24(7), 1199-1214,
519 <https://doi.org/10.1175/JTECH2033.1>, 2007.

520 Kovalev, V. A., Newton, J., Wold, C., Wei, M.: Simple algorithm to determine the near-edge smoke boundaries with
521 scanning lidar, *Appl. Optics.*, 44(9), 1761-1768, <https://doi.org/10.1364/ao.44.001761>, 2005.

522 Kuji, M.: Retrieval of water cloud top and bottom heights and the validation with ground-based observations, *Proc.*
523 *SPIE-Int. Soc. Opt. Eng.*, 8890, 88900R, <https://doi.org/10.1117/12.2029169>. 2013.

524 Li, J., Yi, Y., Stamnes, K., Ding, X., Wang, T., Jin, H., and Wang, S.: A new approach to retrieve cloud base height
525 of marine boundary layer clouds, *Geophys. Res. Lett.*, 40(16), 4448-4453, <https://doi.org/10.1002/grl.50836>,
526 2013.

527 Lohmann, U., and Gasparini, B.: A cirrus cloud climate dial?, *Science.*, 357(6348), 248-249,
528 <https://doi.org/10.1126/science.aan3325>, 2017.

529 Luke, E. P., Kollias, P., Johnson, K. L., and Clothiaux, E. E.: A technique for the automatic detection of insect
530 clutter in cloud radar returns, *J. Atmos. Ocean. Tech.*, 25(9), 1498-1513,
531 <https://doi.org/10.1175/2007JTECHA953.1>, 2008.

532 Mao, F., Gong, W., and Zhu, Z.: Simple multiscale algorithm for layer detection with lidar, *Appl. Optics.*, 50(36),
533 6591-6598, <https://doi.org/10.1364/AO.50.006591>, 2011.

534 Melnikov, V. M., Istok, M. J., and Westbrook, J. K.: Asymmetric radar echo patterns from insects, *J. Atmos. Ocean.*
535 *Tech.*, 32(4), 659-674, <https://doi.org/10.1175/JTECH-D-13-00247.1>, 2015.

536 Melnikov, V., Leskinen, M., and Koistinen, J.: Doppler velocities at orthogonal polarizations in radar echoes from
537 insects and birds, *IEEE. Geosci. Remote. S.*, 11(3), 592-596, <https://doi.org/10.1109/LGRS.2013.2272011>, 2013.

538 Morille, Y., Haeffelin, M., Drobinski, P., and Pelon, J.: STRAT: An automated algorithm to retrieve the vertical
539 structure of the atmosphere from single-channel lidar data, *J. Atmos. Ocean. Tech.*, 24(5), 761-775,
540 <https://doi.org/10.1175/JTECH2008.1>, 2007.

541 Moty, G. S., Satyanarayana, M., Jayeshlal, G. S., Krishnakumar, V., and Mahadevan, Pillai, V. P.: Lidar observed
542 structural characteristics of higher altitude cirrus clouds over a tropical site in Indian subcontinent region, *J.*

543 Atmos. Sol.-Terr. Phys., 179, 367-377, [https://doi.org/ 10.1016/j.jastp.2018.08.013](https://doi.org/10.1016/j.jastp.2018.08.013), 2018.

544 Nakajima, T., and King, M. D.: Determination of the optical thickness and effective particle radius of clouds from
545 reflected solar radiation measurements. Part I: Theory, *J. Atmos. Sci.*, 47(15), 1878-1893,
546 [https://doi.org/10.1175/1520-0469\(1990\)047%3C1878:DOTOTA%3E2.0.CO;2](https://doi.org/10.1175/1520-0469(1990)047%3C1878:DOTOTA%3E2.0.CO;2), 1990.

547 Oh, S. B., Kim, Y. H., Kim, K. H., Cho, C. H., and Lim, E.: Verification and correction of cloud base and top height
548 retrievals from Ka-band cloud radar in Boseong, Korea, *Adv. Atmos. Sci.*, 33(1), 73-84, [https://doi.org/](https://doi.org/10.1007/s00376-015-5058-y)
549 [10.1007/s00376-015-5058-y](https://doi.org/10.1007/s00376-015-5058-y), 2016.

550 Pal, S. R., Steinbrecht, W., and Carswell, A. I.: Automated method for lidar determination of cloud-base height and
551 vertical extent, *Appl. Optics.*, 31(10), 1488-1494, <https://doi.org/10.1364/AO.31.001488>, 1992.

552 Platt, C. M., Young, S. A., Carswell, A. I., Pal, S. R., McCormick, M. P., Winker, D. M., Delguasta, M., Stefanutti,
553 L., Eberhard, W. L., Hardesty, M., Flamant, P. H., Valentin, R., Forgan, B., Gimmetstad, G. G., Jäger, H.,
554 Khmelevtsov, S. S., Kolev, I., Kaprieolev, B., Lu, D., Sassen, K., Shamanaev, V. S., Uchino, O., Mizuno, Y.,
555 Wandinger, U., Weitkamp, C., Ansmann, A., and Wooldridge, C.: The experimental cloud lidar pilot study
556 (ECLIPS) for cloud-radiation research, *B. Am. Meteorol. Soc.*, 75(9), 1635-1654,
557 [https://doi.org/10.1175/1520-0477\(1994\)075<1635:TECLPS>2.0.CO;2](https://doi.org/10.1175/1520-0477(1994)075<1635:TECLPS>2.0.CO;2), 1994.

558 Protat, A., Delanoe, J., May, P. T., Haynes, J., Jakob, C., O'Connor, E., Pope, M., and Wheeler, M. C.: The
559 variability of tropical ice cloud properties as a function of the large-scale context from ground-based radar-lidar
560 observations over Darwin, Australia, *Atmos. Chem. Phys.*, 11, 8363-8384,
561 <https://doi.org/10.5194/acp-11-8363-2011>, 2011.

562 Riddle, A. C., Gage, K. S., Balsley, B. B., Ecklund, W. L., and Carter, D. A.: Poker Flat MST Radar Data Bases,
563 NOAA Tech. Memorandum. ERL AL-11., <https://repository.library.noaa.gov/view/noaa/21227>, 1989.

564 Sassen, K., and Mace, G.: Ground-based Remote Sensing of Cirrus Clouds, Oxford University Press., 168-196,
565 <https://doi.org/10.1093/oso/9780195130720.003.0012>, 2001.

566 Sauvageot, H.: Retrieval of vertical profiles of liquid water and ice content in mixed clouds from Doppler radar and
567 microwave radiometer measurements, *J. Appl. Meteorol. Clim.*, 35(1), 14-23,
568 [https://doi.org/10.1175/1520-0450\(1996\)035%3C0014:ROVPOL%3E2.0.CO;2](https://doi.org/10.1175/1520-0450(1996)035%3C0014:ROVPOL%3E2.0.CO;2), 1996.

569 Sherwood, S. C., Bony, S., and Dufresne, J. L.: Spread in model climate sensitivity traced to atmospheric
570 convective mixing, *Nature.*, 505(7481), 37-42, <https://doi.org/10.1038/nature12829>, 2014.

571 Shupe, M. D., Kollias, P., Poellot, M., and Eloranta, E.: On deriving vertical air motions from cloud radar Doppler
572 spectra, *J. Atmos. Ocean. Tech.*, 25(4), 547-557, <https://doi.org/10.1175/2007JTECHA1007.1>, 2008.

573 Stephens, G. L., Li, J., Wild, M., Clayson, C. A., Loeb, N., Kato, S., L'ecuyer, T., Stackhouse, Jr, P. W., Lebsock,
574 M., and Andrews, T.: An update on Earth's energy balance in light of the latest global observations, *Nat. Geosci.*,
575 5(10), 691-696, <https://doi.org/10.1038/ngeo1580>, 2012.

576 Stephens, Graeme. L.: Cloud Feedbacks in the Climate System: A Critical Review, *J. Climate.*, 18(2), 237-273,
577 <https://doi.org/10.1175/JCLI-3243.1>, 2005.

578 Streicher, J., Werner, C., Köepp, F.: Verification of lidar visibility, cloud base height, and vertical velocity
579 measurements by laser remote sensing, *SPIE.*, 2506, 576-579, <https://doi.org/10.1117/12.221061>, 1995.

580 Thorsen, T. J., Fu, Q., and Comstock, J. M.: Cloud effects on radiative heating rate profiles over Darwin using
581 ARM and A-train radar/lidar observations, *J. Geophys. Res-Atmos.*, 118(11), 5637-5654,

582 <https://doi.org/10.1002/jgrd.50476>, 2013.

583 Varikoden, H., Harikumar, R., Vishnu, R., Sasi Kumar, V., Sampath, S., Murali Das, S., and Mohan Kumar, G.:
584 Observational study of cloud base height and its frequency over a tropical station, Thiruvananthapuram, using a
585 ceilometer, *Int. J. Remote. Sens.*, 32(23), 8505-8518, <https://doi.org/10.1080/01431161.2010.542199>, 2011.

586 Veselovskii, I., Goloub, P., Podvin, T., Tanre, D., Ansmann, A., Korenskiy, M., Borovoi, A., Hu, Q., and Whiteman,
587 D. N.: Spectral dependence of backscattering coefficient of mixed phase clouds over West Africa measured with
588 two-wavelength Raman polarization lidar: Features attributed to ice-crystals corner reflection, *J. Quant.*
589 *Spectrosc. Ra.*, 202, 74-80, <https://doi.org/10.1016/j.jqsrt.2017.07.028>, 2017.

590 Wandinger, U.: Introduction to Lidar, Brooks/Cole Pub Co, https://doi.org/10.1007/0-387-25101-4_1, 2005.

591 Wang, J., and Rossow, W. B.: Determination of cloud vertical structure from upper-air observations, *J. Appl.*
592 *Meteorol. Clim.*, 34(10), 2243-2258,
593 [https://doi.org/10.1175/1520-0450\(1995\)034%3C2243:DOCVSF%3E2.0.CO;2](https://doi.org/10.1175/1520-0450(1995)034%3C2243:DOCVSF%3E2.0.CO;2), 1995.

594 Wang, J., and Rossow, W. B.: Effects of cloud vertical structure on atmospheric circulation in the GISS GCM, *J.*
595 *Climate.*, 11(11), 3010-3029, [https://dx.doi.org/10.1175/1520-0442\(1998\)011%3C3010:EOCVSO%3E2.0.CO;2](https://dx.doi.org/10.1175/1520-0442(1998)011%3C3010:EOCVSO%3E2.0.CO;2),
596 1998.

597 Wang, Z.: Cloud property retrieval using combined ground-based remote sensors, The University of Utah, 2000.

598 Ward, J. G., and Merceret, F. J.: An automated cloud-edge detection algorithm using cloud physics and radar data, *J.*
599 *Atmos. Ocean. Tech.*, 21(5), 762-765,
600 [https://doi.org/10.1175/1520-0426\(2004\)021%3C0762:AACDAU%3E2.0.CO;2](https://doi.org/10.1175/1520-0426(2004)021%3C0762:AACDAU%3E2.0.CO;2), 2004.

601 Wild, M.: New Directions: A facelift for the picture of the global energy balance, *Atmos. Environ.*, 55(none),
602 366-367, <https://doi.org/10.1016/j.atmosenv.2012.03.022>, 2012.

603 Williams, C. R., Bringi, V. N., Carey, L. D., Chandrasekar, V., Gatlin, P. N., Haddad, Z. S., Meneghini, R., Munchak,
604 S. J., Nesbitt, S. W., Petersen, W. A., Tanelli, S., Tokay, A., Wilson, A., and Wolff, D. B.: Describing the shape of
605 raindrop size distributions using uncorrelated raindrop mass spectrum parameters, *J. Appl. Meteorol. Clim.*,
606 53(5), 1282-1296, <https://doi.org/10.1175/JAMC-D-13-076.1>, 2014.

607 Xie, H., Zhou, T., Fu, Q., Huang, J., Huang, Z., Huang, Z., Bi, J., Shi, J., Zhang, B., and Ge, J.: Automated
608 detection of cloud and aerosol features with SACOL micro-pulse lidar in northwest China, *Opt. Express.*, 25(24),
609 30732-30753, <https://doi.org/10.1364/OE.25.030732>, 2017.

610 Young, S. A.: Analysis of lidar backscatter profiles in optically thin clouds, *Appl. Optics.*, 34(30), 7019-7031,
611 <https://doi.org/10.1364/AO.34.007019>, 1995.

612 Zhang, J., Chen, H., Xia, X., and Wang, W.: Dynamic and thermodynamic features of low and middle clouds
613 derived from atmospheric radiation measurement program mobile facility radiosonde data at Shouxian, China,
614 *Adv. Atmos. Sci.*, 33(1), 21-33, <https://doi.org/10.1007/s00376-015-5032-8>, 2016.

615 Zhang, L., Dong, X., Kennedy, A, Xi, B., and Li, Z.: Evaluation of NASA GISS post-CMIP5 single column model
616 simulated clouds and precipitation using ARM Southern Great Plains observations, *Adv. Atmos. Sci.*, 34(3),
617 306-320, <https://doi.org/10.1007/s00376-016-5254-4>, 2017.

618 Zhang, Y., Zhang, L., Guo, J., Feng, J., Cao, L., Wang, Y., Zhou, Q., Li, L., Li, B., Xu, H., Liu, L., An, N., and Liu,
619 H.: Climatology of cloud-base height from long-term radiosonde measurements in China, *Adv. Atmos. Sci.*,
620 35(2), 158-168, <https://doi.org/10.1007/s00376-017-7096-0>, 2018.

621 Zhao, C., Wang, Y., Wang, Q., Li, Z., Wang, Z., and Liu, D.: A new cloud and aerosol layer detection method based
622 on micropulse lidar measurements, *J. Geophys. Res-Atmos.*, 119(11), 6788-6802,
623 <https://doi.org/10.1002/2014JD021760>, 2014.

624 Zheng, J., Zhang, J., Zhu, K., Liu, L., and Liu, Y.: Gust front statistical characteristics and automatic identification
625 algorithm for CINRAD, *J. Meteorol. Res-Prc.*, 28(4), 607-623, <https://doi.org/10.1007/s13351-014-3240-2>,
626 2014.

627 Zhou, C., Zelinka, M. D., and Klein, S. A.: Impact of decadal cloud variations on the Earth's energy budget, *Nat.*
628 *Geosci.*, <https://doi.org/10.1038/ngeo2828>, 2016.

629 Zhou, Q., Zhang, Y., Li, B., Li, L., Feng, J., Jia, S., Lv, S., Tao, F., and Guo, J.: Cloud-base and Cloud-top Heights
630 Determined from a Ground-based Cloud Radar in Beijing, China, *Atmos. Environ.*, 201(MAR.), 381-390,
631 <https://doi.org/10.1016/j.atmosenv.2019.01.012>, 2019.